


## RESEARCH ARTICLE

# The stress–strain behavior of refractory microcracked aluminum titanate: The effect of zigzag microcracks and its modeling

Mossaab Mouiya<sup>1,2</sup> | Mikhail Martynyuk<sup>3</sup> | Andreas Kupsch<sup>4</sup> | René Laquai<sup>4,5</sup> | Bernd R. Müller<sup>4</sup> | Nicolas Tessier Doyen<sup>1</sup> | Youssef Tamraoui<sup>2</sup> | Itziar Serrano-Munoz<sup>4</sup> | Marc Huger<sup>1</sup> | Mark Kachanov<sup>6</sup> | Giovanni Bruno<sup>4,7</sup> 

<sup>1</sup>IRCER, Centre Européen de la Céramique (CEC), Limoges Cedex, France

<sup>2</sup>Materials Science, Energy and Nanoengineering Department, Mohammed VI Polytechnic University (UM6P), Ben Guerir, Morocco

<sup>3</sup>Nizhny Novgorod State Technical University named after R.E. Alekseev, Nizhny Novgorod, Russia

<sup>4</sup>Bundesanstalt für Materialforschung und -prüfung (BAM), Berlin, Germany

<sup>5</sup>Physikalisch-Technische Bundesanstalt (PTB), Braunschweig, Germany

<sup>6</sup>Department of Mechanical Engineering, Tufts University, Medford, Massachusetts, USA

<sup>7</sup>Department of Physics and Astronomy, University of Potsdam, Potsdam, Germany

## Correspondence

Giovanni Bruno, Bundesanstalt für Materialforschung und -prüfung (BAM), Unter den Eichen 87, 12205 Berlin, Germany.  
Email: [Giovanni.bruno@bam.de](mailto:Giovanni.bruno@bam.de)

## Funding information

French National Research Agency's, Grant/Award Number: ANR 19 CE09 0035; Deutsche Forschungsgemeinschaft, Grant/Award Number: DFG 431178689

## Abstract

The stress–strain behavior of ceramics, such as aluminum titanate, has certain features that are unusual for brittle materials—in particular, a substantial nonlinearity under uniaxial tension, and load–unload hysteresis caused by the sharp increase of the incremental stiffness at the beginning of unloading. These features are observed experimentally and are attributed to microcracking. Here we compare different degrees of stress–strain nonlinearity of aluminum titanate materials and quantitatively model them. We use advanced mechanical testing to observe the mechanical response at room and high temperature; electron microscopy, and X-ray refraction radiography to observe the microstructural changes. Experiments show that two types of microcracks can be distinguished: (i) microcracks induced by cooling from the sintering temperature (due to heterogeneity and anisotropy of thermal expansion), with typical sizes of the order of grain size, and (ii) much larger microcracks generated by the mechanical loading. The two microcrack types produce different effects on the stress–strain curves. Such microcracks and the features of the stress–strain behavior depend on the density of the cooling-induced microcracks and on the distribution of grain sizes. They are modeled analytically and numerically.

## KEYWORDS

hysteresis, nonlinear stress–strain curve, refractory, stiffness, X-ray refraction

This is an open access article under the terms of the [Creative Commons Attribution](https://creativecommons.org/licenses/by/4.0/) License, which permits use, distribution and reproduction in any medium, provided the original work is properly cited.

© 2023 The Authors. *Journal of the American Ceramic Society* published by Wiley Periodicals LLC on behalf of American Ceramic Society.

## 1 | INTRODUCTION

Ceramics are known as high-strength, stiff but brittle materials. If the brittleness could be overcome, it would be possible to expand the applications of ceramics. On the other hand, the reduction of stiffness due to microcracking allows other applications. Flexible ceramics could be used as anti-vibration materials and in the refractory field as thermal shock resistant materials. Microcracking is caused, in particular, by cooling from the sintering temperature, due to the heterogeneity and anisotropy of its thermal expansion. Aluminum titanate  $\text{Al}_2\text{TiO}_5$  (AT) has found an increasing number of applications as an engineering ceramic material in different areas and it turns out to be one of the most interesting microcracked ceramics, so it is chosen here as the material to study. According to Bayer,<sup>1</sup> the thermal expansion coefficients (from room temperature [RT] to  $1000^\circ\text{C}$ ) along the crystallographic directions are highly anisotropic:  $\alpha_a = -2.9 \times 10^{-6} \text{ K}^{-1}$ ,  $\alpha_b = 10.3 \times 10^{-6} \text{ K}^{-1}$ , and  $\alpha_c = 20.1 \times 10^{-6} \text{ K}^{-1}$ ; note that one of them is negative.

These intrinsic properties (microcracking, negative thermal expansion, and others we will encounter later) make AT an excellent candidate ceramic material to obtain a quasi-ductile fracture behavior at elevated temperature.<sup>2</sup> The instability of the AT compound (i.e., its tendency to decompose in alumina and titania) over the temperature range of  $\sim 800\text{--}1280^\circ\text{C}$  and its low strength are among of its disadvantages. Accordingly, several additives have been employed with different efficiencies for stabilizing microstructures through a eutectoid reaction.<sup>3</sup>

The low strength and stiffness are largely attributed to extensive microcracking occurring during cooling from the sintering temperature, due to the abovementioned anisotropy of the thermal expansion. The microcracks have diverse, “irregular” shapes. This complicates an estimation of their effect on the overall elastic properties. The first challenge is that the usual crack density parameter introduced by Bristow,<sup>4</sup>  $\rho = (1/V) \sum_k a_k^3$  ( $a_k$  are cracks' radii, and  $V$  is the reference volume; the value of  $\rho$  can be visualized as follows:  $(4\pi/3)\rho$  is the relative volume of spheres circumscribed about circular cracks), is not even defined for noncircular cracks. On the other hand, this parameter reflects two features relevant for cracks of any shape: (1) their contributions to the effective elastic properties scale as their linear sizes cubed; hence, only the largest microcracks have to be taken into account (much smaller cracks can be ignored unless they outnumber the larger ones by orders of magnitude); (2) crack openings and hence “crack porosity” are irrelevant for the elastic properties and hence do not need to be known, provided that they are small. These features are beneficial for the processing of microphotographic data.

**TABLE 1** Sintering conditions and resulting density/porosity for AT materials referenced non-flexible (NF), flexible (F), and very flexible (VF).

Material references	NF	F	VF
Type of sintering	Natural (pressureless)		
Temperature ( $^\circ\text{C}$ )	1500	1600	1600
Dwell time (h)	1	2	8
Apparent density ( $\text{g}/\text{cm}^3$ )	3.32	3.21	3.16
Relative density (%)	93.4	90.4	89.1
Open porosity (%)	4.5	8.3	9.1
Microcrack volume fraction (%)	2.4	3.0	3.1

The cooling-induced microcracks follow polyhedral (polygonal in 2D) grain boundaries, with occasional intersections. As discussed in the text to follow, the larger, loading-induced microcracks tend to have zigzag shapes. Such geometries have been discussed by Gao et al.<sup>5</sup> and by Bruno et al.,<sup>6</sup> as they play an important role for the behavior of such ceramics under uniaxial tension. The compliance contribution of zigzag cracks has been recently analyzed by Martynyuk and Kachanov.<sup>7</sup>

In the present study, three types of AT materials, with different amounts of microcracking, were used as model refractory materials, and their behavior was investigated experimentally and modeled by micromechanical (analytical and numerical) approaches.

## 2 | MATERIALS AND METHODS

### 2.1 | Aluminum titanate doped with silica

Granulated industrial powder (TM-20P) was used to produce the AT materials by uniaxial pressing. Different sintering temperatures, dwell time, and cooling rates were applied (see Table 1) in order to produce different types of microstructures (in terms of grain size, microcracking, and grain boundary features), mimicking the microstructure of itacolumite, a widely used refractory.

Three different materials were examined: NF (non-flexible, small grain size), F (flexible), and VF (very flexible, large grain size). Although they had porosity below 10%, they showed different mechanical behaviors (note that such porosity is open, and no isolated pores were observed). The obtained apparent density (obtained by dividing the weight by the measured volume) is about  $3.2 \text{ g}/\text{cm}^3$  for all specimens, showing that the densification is identical during their respective sintering cycles. For the NF material, a lower temperature and shorter soaking

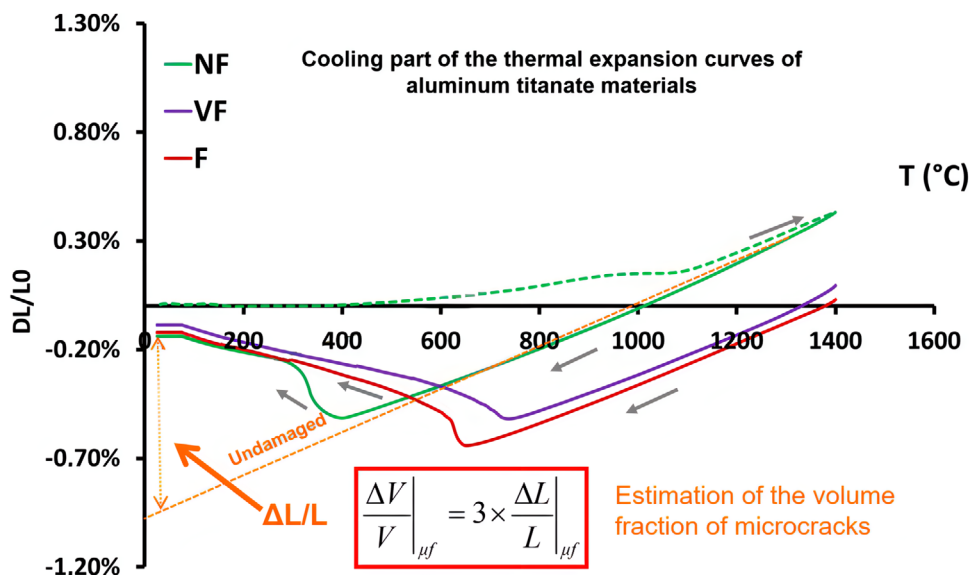


FIGURE 1 Cooling branch of the relative dilation curve as a function of temperature and estimation of the microcrack volume. The details of the dilation measurements are given in Section 3.

time were used to prevent grain growth, whereas VF samples were subjected to higher temperature and longer heat treatment to promote grain coarsening. F samples were produced at intermediate soaking time, but high temperature. After sintering, the density and open pores volume fraction were measured using Archimedes' method (water as test fluid). The results show that NF samples had the highest relative density (93.4%), whereas VF samples had the lowest one (89.1%).

*Remark.* In the sintering process, the level of compaction should increase with the temperature and with the sintering time. This is, however, true only initially; later, when the sintering temperature becomes too high and/or sintering is carried out for a very long time, a de-densification may occur. Such loss of compaction can be the result of pore trapping and/or grain coarsening. In the case of AT materials, grain coarsening promotes microcracking during cooling, and this produces additional porosity, as determined by thermal expansion curves (see below).

Therefore, in our case, microcracks are responsible for the increase of porosity from NF to VF. Although microcracks have crack-opening-displacements of sub-micrometric or even nanometric size, their total volume fraction can be estimated using various techniques such as thermal expansion measurements.

The procedure has been first suggested by Ohya and Nakagawa<sup>8</sup> and consists of prolonging from high to room temperature (RT) the cooling branch of the relative dilation curve (DL/LO vs. T) (Figure 1), and taking the difference to the dilation measured at RT. The volume of the microcracks generated during cooling can be estimated as  $3 \times DL/LO$  (analogous to the calculation of the

hydrostatic strain through the trace of the strain tensor) and is reported in Table 1 that summarizes microstructural features and sintering parameters.

### 3 | EXPERIMENTAL TECHNIQUES

#### 3.1 | Linear dilation

Dilatometric measurements were conducted using a horizontal dilatometer (DIL 402 PC, Netzsch, Selb, Germany). The sample had a prismatic shape ( $5 \times 5 \times 25 \text{ mm}^3$ ). It was tested in air, starting from RT to  $1400^\circ\text{C}$  and then cooled back to RT, at heating and cooling rates of  $5^\circ\text{C}/\text{min}$ .

#### 3.2 | Uniaxial tensile test

Tensile tests on an INSTRON 8862 electromechanical universal testing machine were carried out to investigate the stress-strain behavior of AT samples at RTs (Figure 2). Starting from a large sintered prismatic block, a cylinder of 180 mm in length and 20 mm in diameter was first extracted by core drilling. Then, two metallic bases were glued at each end of the sample. The samples, with the two metallic bases, were then machined together (with a fine diamond-based grinding wheel) in order: (i) to obtain a dog bone cylinder with a central diameter of 16 mm and (ii) to avoid unwanted geometrical defects. No additional polishing was performed. The testing machine shown in Figure 2 was designed for incremental cyclic tensile tests. During these tests, the sample was loaded in load-control

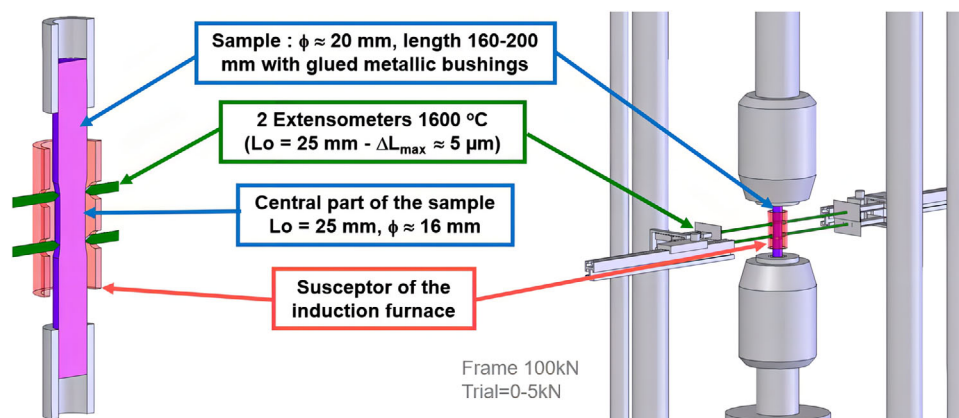


FIGURE 2 Schematics of the tensile test device. See also Ref. [9].

mode at a rate of 0.01 kN/s until the load reached approximately 100 N (equivalent to 0.5 MPa). Then, we switched to displacement control mode and carried on the test at a rate of 0.001 mm/s, until the displacement reached  $0.002 \text{ mm} + (n - 1) \times 0.001 \text{ mm}$ , where  $n$  represents the cycle number. Unloading was always carried out in load-control mode.

Precise strain measurements were obtained by two capacitive extensometers equipped with SiC rods, located on the opposite sides of the sample. To enable testing under a controlled atmosphere (air, argon), the extensometers are covered by sealed water-cooled casings, see Ref. [9].

### 3.3 | Microscopy

The microstructure was examined using a scanning electron microscope (FEI ESEM Quanta 450 FEG, FEI) operated with a 10–30 kV accelerating voltage. Sample cross sections of  $10 \times 10 \text{ mm}^2$  were prepared according to common grinding and polishing protocol in order to achieve a planar surface while limiting grain debonding. Grain size distributions were assessed by analyzing SEM images using ImageJ software (version 1.52v).

### 3.4 | X-ray refraction radiography

Synchrotron X-ray refraction<sup>10,11</sup> radiography (SXRR) measurements were carried out at the BAM synchrotron laboratory BAMline at Helmholtz-Zentrum Berlin, Germany<sup>12–14</sup> according to the diffraction enhanced imaging principle.<sup>15,16</sup> Contrary to absorption-based radiography, SXRR is particularly sensitive to internal interfaces (cracks, pores, phase boundaries, etc.). SXRR has been used successfully to characterize microcracks or damage in ceramics.<sup>17–20</sup> In situ SXRR studies revealed

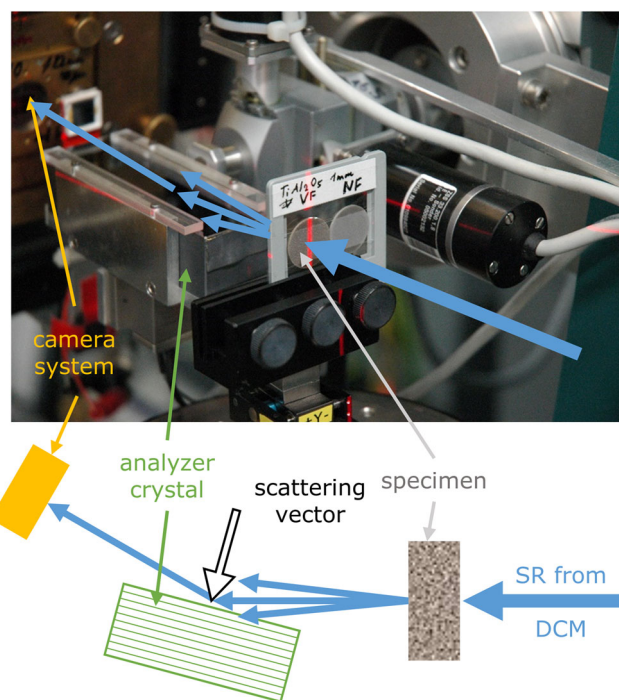


FIGURE 3 Experimental setup of the X-ray refraction station at BAMline. The blue arrows indicate the beam path of the synchrotron radiation (SR). The specimens are mounted in a slide frame shown on the right. A sketch of the setup is shown at the bottom.

the evolution of damage of composite materials under external load<sup>21,22</sup> or the evolution of an alloy's porosity during heat treatment.<sup>23</sup> Very recently, SXRR was employed as input data for 3D computed tomography studies.<sup>24,25</sup>

The AT specimens were mounted in a slide frame as shown in Figure 3. A double crystal (Si (111)) monochromator was used to extract a highly collimated monochromatic X-ray beam (band width  $\sim 0.2\%$ ).

The beam energy was set to 17.5 keV to achieve a specimen X-ray transmission of about 15%. A Princeton Instruments camera (2048 × 2048 pixel) in combination with a lens system and a 50 μm thick CdWO<sub>4</sub> scintillator screen provided a pixel size of 3.5 μm × 3.5 μm, capturing a field of view of about 7 mm × 7 mm.<sup>26</sup> The incident beam was narrowed to the field of view by a slit system to suppress detector backlighting.<sup>27,28</sup> An Si (111) analyzer crystal (AC) was placed in the beam path between the specimen and the camera system (Figure 3). When aligned to the Bragg angle ( $\theta_B = 6.48744^\circ$ ), the AC reflects the synchrotron radiation beam into the detector system. By slightly tilting the AC in the vicinity of  $\theta_B$  (here: 81 steps with  $\Delta\theta = 2 \times 10^{-4}^\circ$ , exposure time 2 s), a so-called rocking curve (RC) is recorded. Relative to the intrinsic RC (without specimen), specimens having internal interfaces dampen the RC's peak height and broaden its width significantly (and possibly shift its center). These parameters were evaluated using an in-house software code<sup>29</sup> based on Python. For example, for the VF specimen, the full width half maximum of about  $0.00094^\circ$  of the intrinsic RC was increased to  $0.00214^\circ$ . By using the image processing software Fiji Image J,<sup>30</sup> the attenuation ( $\mu \cdot d$ ) and the refraction value ( $C_m \cdot d$ ) were evaluated for each pixel according to Equations (1) and (2), respectively. To eliminate the dependency on thickness, the specific surface  $C_m/\mu$  was calculated. Thus,

$$\mu \cdot d = -\ln\left(\frac{I}{I_0}\right) \quad (1)$$

$$C_m \cdot d = 1 - \frac{I_R}{I_{R0}} \cdot \frac{I_0}{I} \quad (2)$$

where  $d$  is the specimen's thickness,  $I$  and  $I_R$  are the RC's integral and peak height, respectively, with the specimen in the beam, and  $I_0$  and  $I_{R0}$  are the respective quantities without a specimen in the beam. A detailed description of data conditioning and evaluation can be found in Refs. [21, 29, 31].

### 3.5 | Ultrasound resonance

In-house developed ultrasound resonance equipment (at IRCER) was used to determine Young's modulus of the materials as a function of temperature up to 1400°C (the heating rate was 5°C/min). The waves emitted by the transducer propagate through the sample via an alumina waveguide as illustrated in Figure 4. The guide-sample interface and the end of the sample create different reflection echoes, which allow the measurement of the flight time of the longitudinal wave ( $\tau$ ), from which Young's modulus can be calculated according to

$$E = \delta (2L/\tau)^2 \quad (3)$$

where  $\delta$  is the bulk density of the material,  $L$  the length of the sample, and  $\tau$  the round-trip time for the longitudinal wave.

## 4 | EXPERIMENTAL RESULTS

Typical microstructures of the materials prior to testing are shown in Figure 5 (SEM pictures). Large differences are seen between non-flexible (NF) and flexible samples (F and VF). The NF sample shows a relatively homogeneous grain size distribution, with small grain sizes. In contrast, F and VF samples exhibited more heterogeneous grain size distributions, with some very large grains, especially in VF. Microcracks were abundant in VF samples, and they tended to be larger (following Cleveland and Bradt's ansatz<sup>32,33</sup> for oxide materials, also confirmed by Ohya and Nakagawa<sup>8</sup> for non-oxide ceramics), as well as a silica interphase; both were also present in F.

Each micrograph exhibits three distinct phases (Figure 5): (i) medium-gray AT phase (grains), (ii) dark-gray vitreous bonding phase (surrounding the grains), and (iii) dark (black) microcracks, primarily intergranular, as well as pores. (Note that some of the pores may form at the sites of grains that have been stripped away during the polishing procedure.)

Mechanical loading leads to the appearance of relatively long zigzag cracks (Figure 6). They tend to be parallel to the rupture surface, that is, normal to the loading direction,<sup>19</sup> and hence, their overall effect is anisotropic.

*Remark.* The zigzag cracks seen in Figure 6 may resemble the so-called winged cracks often discussed in geophysical applications (see the review of Lehner and Kachanov<sup>34</sup>), and also in the context of ceramics.<sup>5</sup> The similarity, however, is superficial: The term "winged crack" usually refers to a frictionally sliding crack, with side cracks (wings) growing from its tips, being driven by sliding on the main crack and, on the other hand, being suppressed by the predominantly compressive stress environment. In our case, the propagation mechanism is different—the crack follows grain boundaries, being driven by remotely applied loads, and its geometry differs from the one of a winged crack.

The image analysis of the SEM pictures yields the grain size distribution for the NF, F, and VF samples (the same area is taken in each sample for the evaluation of the number of grains). This is shown in Figure 7. The NF and F samples have a unimodal grain size distribution with a range of sizes from 2 to 20 and 2 to 30 μm, respectively. As the sintering temperature increases, the number of small grains decreases and larger grains become more prominent (see Figures 5 and 7). NF and F samples show grain diameters peaked around 6 and 10 μm and

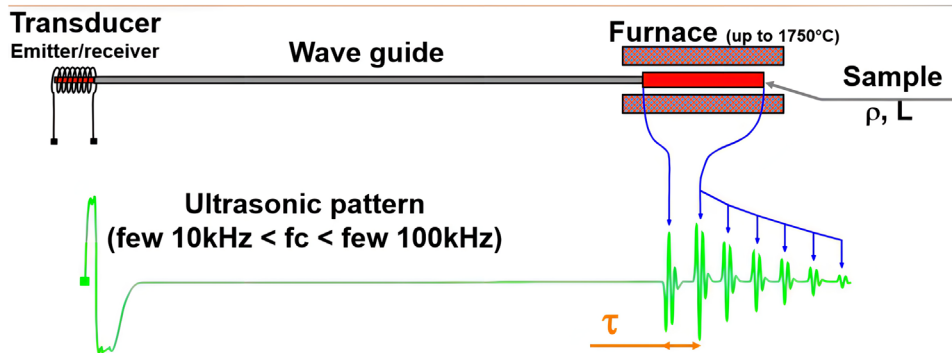


FIGURE 4 Scheme of Young's modulus determination as a function of temperature.

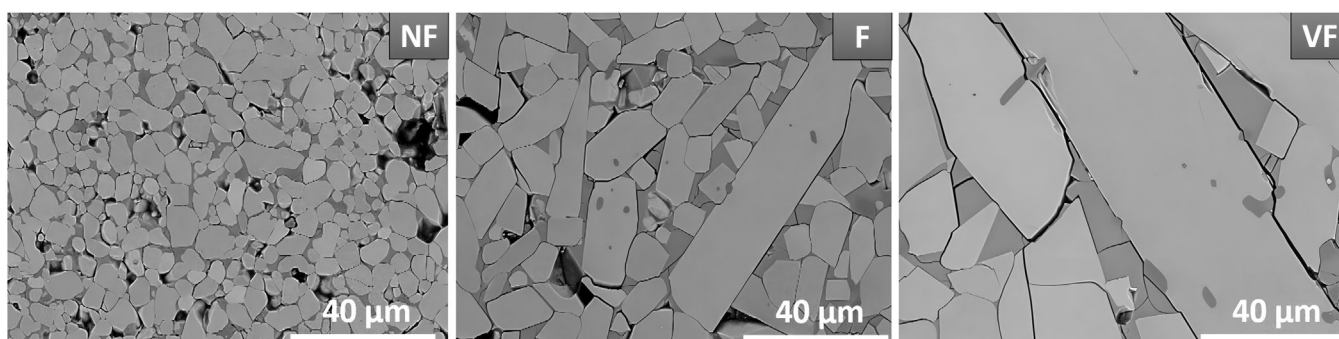


FIGURE 5 Typical microstructures of non-flexible (NF), flexible (F), and very flexible (VF) materials (left to right).

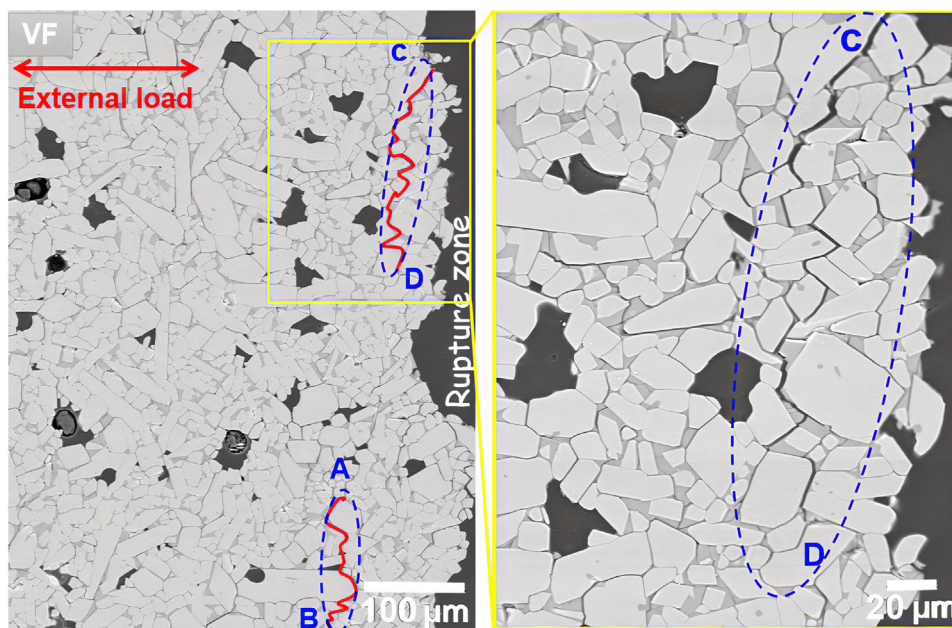


FIGURE 6 Scanning electron microscopy (SEM) picture of the rupture surface (at the right) of sample very flexible (VF), showing subsurface zigzag cracks.

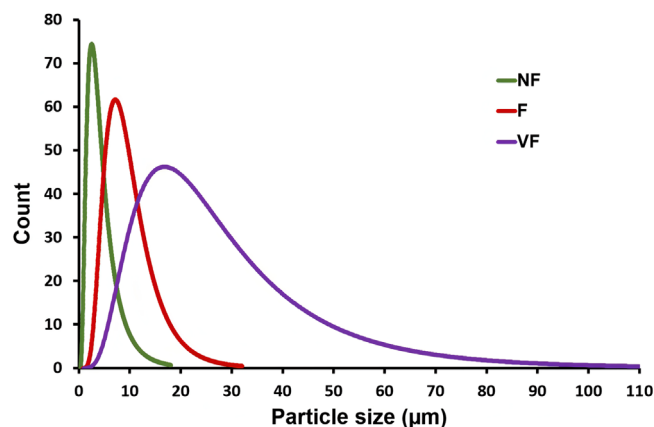


FIGURE 7 Grain size distribution of non-flexible (NF), flexible (F), and very flexible (VF) materials.

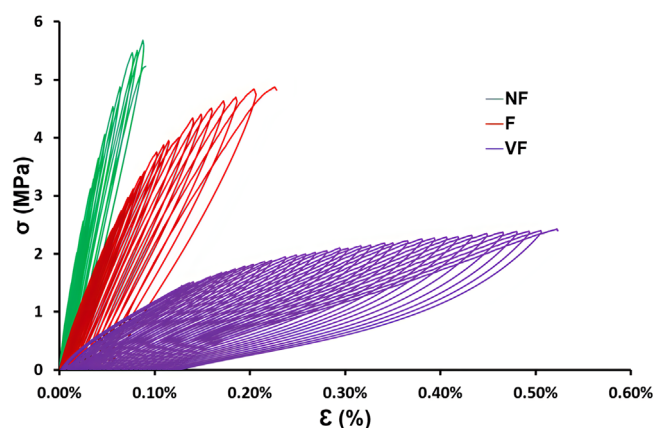


FIGURE 8 The uniaxial cyclic stress–strain curves, for the non-flexible, flexible, and very flexible materials.

maximum grain diameters of 20 and 30  $\mu\text{m}$ , respectively. In contrast, the grain size spread increases with longer sintering times (i.e., in the VF sample sintered at 1600°C for 8 h). The VF sample has an average grain size of approximately 20–30  $\mu\text{m}$  and a maximum size of 110  $\mu\text{m}$ . This illustrates the impact of sintering on microstructural evolution.

The three ceramic materials were tested in uniaxial tension, loading–unloading cycles (Figure 8). Test results are marked by green, red, and purple for the NF, F, and VF compositions, respectively. In all tests, the slope of the stress–strain curve decreases during each loading (indicating progressive damage); at the beginning of unloading, the slope (stiffness) is higher than at the end of loading; this indicates that microcracks get “stuck” and cannot slide back immediately upon unloading (such mechanism has been discussed by Bruno et al.<sup>6</sup>).

The combination between load- and displacement-controlled experiments allowed us to observe possible nonlinear behavior that would be difficult to detect if only

TABLE 2 Mechanical properties of the three materials, as extracted from the uniaxial stress–strain curves (Young’s modulus was extracted at the beginning of loading, in the purely elastic range).

Materials	NF	F	VF
$E$ (GPa)	13.3	6.1	4.6
$\epsilon_{max}$ (%)	0.09	0.22	0.52
$\sigma_{max}$ (MPa)	5.66	4.87	2.42

Abbreviations: F, flexible; NF, non-flexible; VF, very flexible.

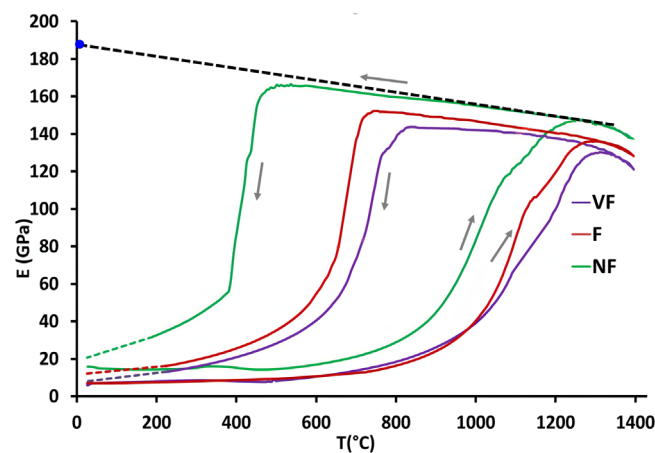
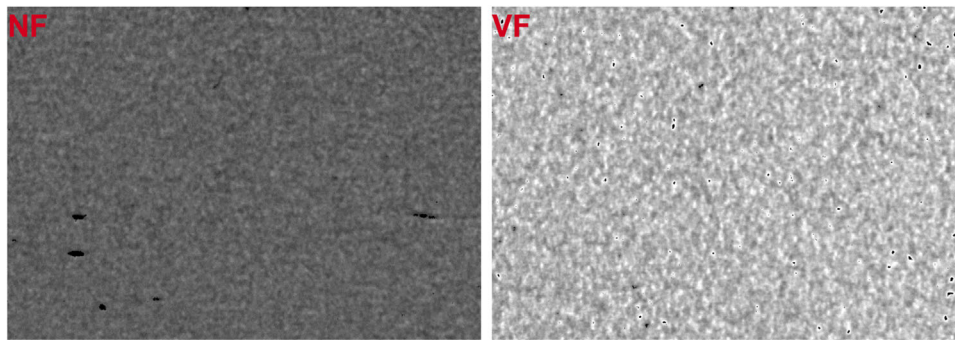


FIGURE 9 Young’s modulus as a function of temperature for all materials investigated. The determination of the undamaged Young modulus is also sketched (dashed black line, see text). The sharp drop corresponds to the onset of microcracking upon cooling.

the load-control modes were utilized. For all NF, F, and VF materials, a nonlinear response was observed. This non-linearity can be attributed to the preexisting microcracks that result from coefficient of thermal expansion (CTE) anisotropy: During loading, these microcracks propagate stably. This diffuse damage leads to a significant increase in strain when the maximum stress at each cycle is reached. The maximum stress at each load–unload cycle is the stress reached at the end of each displacement-controlled cycle, and not the rupture stress.

Table 2 summarizes the mechanical characteristics of the three materials, as extracted from uniaxial testing. The Young modulus of the materials (prior to loading) could be taken from the first cycles of the curves at the beginning of loading.

Young’s modulus was also independently determined as a function of temperature using ultrasound wave reflection, see Figure 4. Figure 9 shows the temperature dependence of Young’s modulus measured by ultrasound resonance, whereas Table 3 shows initial Young’s modulus values, which can be compared with the quantity measured in the uniaxial tests.



**FIGURE 10** X-ray refraction radiographs ( $C_m/\mu$ ) of the non-flexible (NF) and very flexible (VF) samples. Higher gray values (brighter gray tones) indicate a larger internal specific surface. All images are  $3.0 \times 2.1 \text{ mm}^2$ .

**TABLE 3** Young's modulus of the materials investigated, as determined from ultrasonic resonance experiments.

Materials	NF	F	VF
$E$ (GPa)	15.6	7.6	4.8

Abbreviations: F, flexible; NF, non-flexible; VF, very flexible.

Due to the significant CTE mismatch among different crystallographic axes, Young's modulus versus temperature evolution for the three materials (Figure 9) exhibits a pronounced hysteresis. Young's modulus varies greatly between  $25^\circ\text{C}$  (with values close to 10 GPa) and  $1400^\circ\text{C}$  (with values close to 140 GPa), which indicates that the extent of microcracking at RT is very high.

Young's modulus  $E_0$  of the undamaged material at RT was determined by extrapolating the high-temperature linear cooling branch of the  $E$  versus  $T$  curves. In the temperature range prior to the sharp drop (say above  $1200^\circ\text{C}$ ), no microcracks should be present (assuming that they could close or heal at these temperatures, see Refs. [35–40]). From Figure 9, we can infer values of  $E_0$  of 152 GPa for the VF-material to 172 GPa for the F-material, and 185 GPa for the NF one. Thus, the values of  $E_0$  of the bulk undamaged and nonporous material lie in the interval 150–185 GPa.

#### 4.1 | Quantification of microcracking: X-ray imaging

Figure 10 shows the refraction radiographs of the NF and VF specimens (the horizontal ripples are artifacts of the imaging system that could not be eliminated even by the subtraction of reference (so-called flat field) measurements, see above). From the gray values, it is seen that the area of internal surfaces (defects, pores grain boundaries) is higher in the VF specimen than in the NF one (see Table 4). It is well known that the larger the density (surface per unit volume) of defects the larger the X-ray refraction

**TABLE 4** Attenuation and refraction properties (internal specific surface) in very flexible (VF) and non-flexible (NF) samples.

Sample	Spec. surface	Std. deviation	$\mu$ (17.5 keV) ( $\text{mm}^{-1}$ )	Inhomogeneity
NF	0.84	0.04	2.70	0.04
VF	1.13	0.10	2.39	0.11

Note: The standard deviations indicate spatial inhomogeneity and not the experimental error.

signal.<sup>18,41</sup> In our case, this implies a significantly higher microcrack surface in VF.

The attenuation in the NF sample is much higher than of the VF sample; however, this effect is strongly influenced by the thickness of the sample. Importantly, the inhomogeneity (standard deviation of the values throughout the whole field-of-view) of both the X-ray attenuation coefficient (Figure 11) and the specific surface (Figure 10) is higher in the VF sample compared to NF. This implies that VF possesses larger scale features than NF (i.e., larger microcracks).

## 5 | MODELING

The effective stiffness implied by the stress–strain curves is much lower than the stiffness of the bulk (defect-free) material. This fact, plus two other observations: (1) the nonlinearity of the stress–strain behavior resulting in the hysteresis of the RT Young modulus and (ii) the sharp drop of the high-temperature Young modulus at certain point of cooling—can be attributed to progressive microcracking. The following general remarks concerning modeling of cracks should be made.

### 5.1 | Cracks of “irregular” shapes and “equivalent” crack density

The question arises, of quantitative characterization of their density parameter  $\rho$ . As mentioned before, its usual



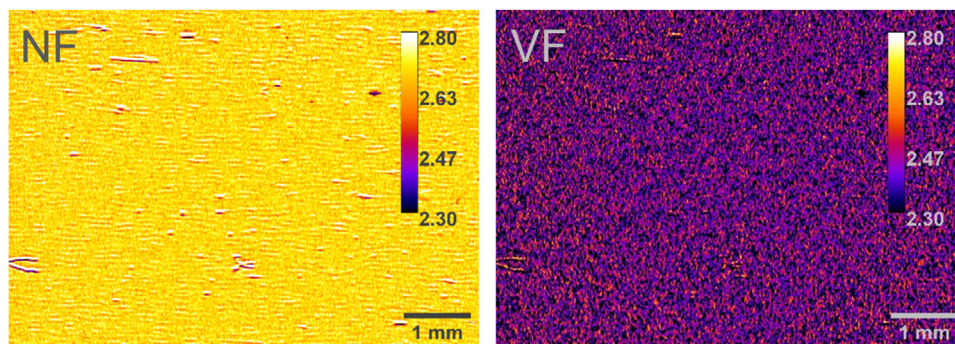


**FIGURE 11** Spatial distribution of the X-ray attenuation coefficient  $\mu$  (at 17.5 keV, in  $\text{mm}^{-1}$ ) in the non-flexible (NF) and very flexible (VF) samples. Brighter yellow tones indicate higher attenuation. All images have a size of  $7.0 \times 5.0 \text{ mm}^2$  (thickness: NF 0.91 mm, VF 0.82 mm).

definition  $\rho = (1/V) \sum_k a_k^3$  assumes that cracks have the circular (penny) shape. Its application to actual noncircular cracks implies—implicitly—that they are replaced by a fictitious set of *circular* cracks that produce the same effect on the overall properties; hence,  $\rho$  can be called the “equivalent” microcrack density. Such equivalent set exists, if microcracks are flat (planar) and their shape irregularities (deviations from circles) are random (see Ref. [42] and the book of Kachanov and Sevostianov<sup>43</sup>); otherwise (strongly non-flat cracks), it may not exist (see Ref. [44]).

This approach is routinely taken—albeit implicitly—in material science applications. Its shortcoming is that the microstructure-property linkage is lost; establishing it would require solving elasticity problems for cracks of “irregular” shapes.<sup>45</sup> Elements of this approach are taken in the present work, namely, in modeling the intergranular cracks generated by cooling; in the present setting, it is justified by the fact that their shapes, being flat, are not known exactly.

We mention yet another observed feature: crack intersections. This factor, however, can be largely ignored, and cracks can be formally treated as nonintersecting, isolated ones, as far as their effect on the overall properties is concerned: Although the intersections affect local stresses near the intersection points, their effect on stress intensity factors and on the overall strain response is rather weak (see the abovementioned book of Kachanov and Sevostianov).

As far as larger zigzag cracks, generated by mechanical loading, are concerned, their effect was analyzed in the recent work of Martynyuk and Kachanov<sup>7</sup>; it is further discussed in the text to follow. Figure 6 shows a photomicrograph of the microstructure of the VF sample after rupture (the broken surface is black [epoxy embedding medium]) where the zigzag cracks are clearly seen.

Thus, the following two types of microcracks, that affect the effective elastic properties, can be distinguished:

- A. Intergranular cracks, of sizes not exceeding the grain dimensions. They are produced by cooling-generated microstresses, due to mismatch of thermal contractions of neighboring grains.
- B. Zigzag cracks formed by the coalescence of intergranular cracks; they are produced by the mechanical loading. Their sizes are much larger than the ones of intergranular cracks.

The values of the effective Young modulus  $E$  observed in the cyclic loading experiments at RT (Table 5) are one-two orders of magnitude lower than its value  $E_0$  for the bulk material (estimated from Figure 9). Such a drastic reduction cannot be explained by the porosity of only a few percent; it can only be attributed to microcracks. We focus on modeling their effect on stiffness.

## 5.2 | Intergranular cracks (Type A)

Their effect cannot be explained in terms of the conventional models of the overall properties of cracked solids. Indeed, these models assume *unrestricted locations* of cracks, whereas intergranular cracking occurs *along grain boundaries*, so that certain *saturation level* of microcrack density  $\rho_*$  exists; it corresponds to fully cracked boundaries (zero stiffness).

The value of  $\rho_*$  is not precisely defined. For example, for cubic grains, the saturation value  $\rho_*$  changes from 0.37 if it is associated with circular cracks on cube faces having diameters equal to cube sides (cracks on neighboring faces touch at one point) to 0.54 if crack diameters are chosen to match crack areas and the areas of cube faces. For elongated shapes—observed in certain proportion of grains (see Figures 5 and 6)—the value of  $\rho_*$  is somewhat larger, as seen from somewhat related 2D examples (with the density of rectilinear cracks of lengths  $2l_k$  defined as  $\rho_{2D} = (1/A) \sum_k l_k^2$  where  $A$  is the reference area): One

TABLE 5 Young's modulus observed in the cyclic loading experiments.

Materials	Instantaneous elastic modulus—first cycle (GPa)			Instantaneous elastic modulus—last cycle (GPa)		
	Beginning of forward loading	End of forward loading	Onset of unloading	Beginning of forward loading	End of forward loading	Onset of unloading
Non-flexible (NF)	13.3	13.5	13.9	12.5	5.7	11.1
Flexible (F)	6.1	5.3	5.8	4.8	1.4	3.8
Very flexible (VF)	4.6	0.8	1.67	1.52	0.4	1.52

obtains  $\rho_* = 0.5$  for square grains increasing to  $\rho_* = 0.83$  for rectangles with aspect ratio 3:1. Overall, the value of  $\rho_* \approx 0.5$  appears to be a reasonable estimate that is used here; note that the results given in the text to follow depend on the ratio  $\rho/\rho_*$  but are relatively insensitive to the exact value of  $\rho_*$ .

A model for the effective elastic properties of a solid with intergranular cracks, which accounts for their saturation level  $\rho_*$ , was developed by Sevostianov and Kachanov.<sup>46</sup> It yields two coupled differential equations for two effective isotropic elastic constants; in cases when Poisson's ratio of the bulk material  $\nu_0 < 0.4$ , it allows an approximate solution for Young's modulus:

$$E/E_0 = (1 - \rho_i/\rho_*)^{D\rho_*} \quad (4)$$

where (if we assume  $\nu_0 = 0.25$ )

$$D = (16/45) (1 - \nu_0^2) (10 - 3\nu_0) / (2 - \nu_0) = 1.76 \quad (5)$$

At small  $\rho$ , the usual non-interaction approximation (NIA) is recovered (where  $\rho_i$  is the "equivalent" intergranular microcrack density, i.e., the density of circular microcracks producing the same effect); at the saturation point  $\rho_i = \rho_*$ ,  $E = 0$ .

If one assumes that the observed drastic reduction of stiffness  $E/E_0$  (Table 5) is entirely due to intergranular microcracks, formula (4) yields the values of  $\rho$  that are very close to the saturation point at maximum loads in last cycles (grain boundaries are almost fully cracked and are close to the breakage point). This does not seem to agree with the photomicrograph data of Figure 6. We recognize, therefore, that much larger zigzag cracks (type B) contribute significantly to the stiffness reduction. It seems reasonable to assume that

- The density of intergranular cracks (produced by cooling) is reflected in the initial slope in forward loading in the first cycle, when loading-induced damage (in the form of larger zigzag cracks) has not occurred, yet;
- Type (B) cracks, formed by the propagation and coalescence of intergranular cracks, are produced by loading. Therefore, the slopes in subsequent cycles reflect the combined effect of the intergranular and the zigzag cracks.

### 5.3 | Zigzag cracks (Type B)

Approximate models of their compliance contributions were developed by Martynyuk and Kachanov,<sup>7</sup> in the framework of 2D modeling. It was found, in particular, that the compliance contribution of a zigzag crack is larger than the one of a rectilinear "shortcut" crack connecting the endpoints of the zigzag. Further, a technique was established of reducing a multi-link zigzag to a set of two-link ones; compliances of the latter were tabulated as functions of the angle variable and constituted the basic building blocks.

In our case, however, a simpler approach to their modeling can be taken, due to the fact that the observed zigzag cracks are long (their length is substantially larger than the amplitude of deviations from the general crack direction) so that they fit inside a narrow ellipse. It is based on the "comparison theorem" of Hill (1963)<sup>47</sup> (see also the book of Kachanov and Sevostianov<sup>43</sup> for discussion in detail) that bounds the compliance contribution of any inhomogeneity by the ones of the circumscribed and inscribed ones (having the same material properties).

Being applied to a zigzag crack, the theorem bounds its compliance contribution by the ones of the rectilinear "shortcut" crack and a circumscribed hole having the shape of a narrow ellipse. The bounds are useful if they are sufficiently tight—as is indeed the case: For an elliptic hole with  $a$  and  $b$  being the larger and the smaller semi-axes, its contribution to the compliance in the normal to the  $a$ -axis direction is proportional to  $2a^2(1 + b/(2a))$ ; the case  $b = 0$  corresponding to the "shortcut" crack.<sup>48</sup> If  $b/a < 0.2$  (a sufficiently narrow ellipse), the normal to the larger axis compliance (the most important compliance component, as zigzag cracks tend to be normal to the loading direction) differs the one of a rectilinear crack of length  $2a$  by less than 10%; hence, it can be estimated, roughly, as the compliance of a rectilinear shortcut crack.

Extending the bounds to a 3D zigzag configuration that fits into a spheroidal pore of narrow opening, its compliance contribution can be estimated, with satisfactory accuracy, by the one of the shortcut cracks. We emphasize that such estimates are sufficiently accurate if the "amplitude" of the zigzag crack is substantially smaller than its length (so that the bounding elliptic pore is narrow).

Many—if not most—of the intergranular cracks appear to fall into this category. Even if such cracks constitute only a fraction of the total number of cracks, they may be responsible for dominant part of the stiffness reduction, as they are larger and the compliance contribution of a crack scales as its linear size *cubed*.

The axial strain contribution of *multiple* zigzag cracks under applied axial stress  $\sigma$  is  $\Delta \varepsilon_z = \sigma(1/E_{eff} - 1/E_0)D\rho_z$ , where  $D$  is defined in Equation (5). Here,  $\rho_z$  is the “equivalent” density of flat cracks (that correspond to oblate circumscribed spheroids, in the limit of zero opening). As  $\rho_z$  appears to be moderately small, not exceeding 0.1–0.2 (the zigzag cracks do not seem to be closely spaced, although more accurate estimates of  $\rho_z$  would require larger field-of-view than typical SEM images), the Non-Interaction Approximation (NIA) is justified for estimates. In its framework, the reduction of Young’s modulus is  $E/E_0 = 1/(1 + D\rho_z)$  (see [49]).

Adding up the compliance contributions of the intergranular and zigzag cracks (of densities  $\rho_i$  and  $\rho_z$ , respectively), their combined effect on the overall stiffness is as follows:

$$E/E_0 = \left[ \left( 1 - \frac{\rho_i}{\rho_*} \right)^{-D\rho_*} + D\rho_z \right]^{-1} \quad (6)$$

It is seen, however, that the additional reduction of stiffness due to the zigzag cracks (the difference between the predictions given by Equations (4) and (6)) is insufficient to explain the data (unless one assumes unrealistically huge values of  $\rho_z$ , first part of Table 5).

Therefore, we explore an alternative approach in modeling the effect of zigzags. As the intergranular cracks are much smaller in size than the zigzags and vastly outnumber them, we first homogenize the effect of the intergranular cracks and then insert the zigzag cracks into the homogenized background. This yields

$$\frac{E}{E_0} = \frac{(1 - \rho_i/\rho_*)^{D\rho_*}}{1 + D\rho_z} \quad (7)$$

Although the predictions given by this formula are closer to the data, Equation (7) still underpredicts the stiffness reduction.

It appears that the mentioned alternative approach—the homogenization of small intergranular microcracks as a background for much larger zigzag cracks—underestimates the compliance contribution of the latter, as shown in 2D simulations, whereby a rectilinear crack was placed in the background of 397 of much smaller cracks, with size contrast (ratio of the size of the large crack and the small surrounding ones) up to 10, see Figure 12. In fact, Figure 12 shows the contribution to the

compliance  $\frac{1}{E_2} = \frac{\varepsilon_{22}}{\sigma_{22}}$  of a large crack placed in a cloud of small cracks.

Numerical simulations were based on the numerical solution (using the Newton–Cotes method) of a system of singular integral equations for pseudo-tractions on cracks (tractions induced on crack lines in a continuous material by the applied load and by the neighboring cracks). After that, the displacement discontinuities on cracks, and their average values were used to determine the crack compliance contributions. For each microcrack density and each contrast of large crack to small crack sizes, 32 microcrack arrays were generated, and the results were averaged over these configurations. The simulations show that the mentioned homogenization exaggerates the compliance contribution of a large crack (by 15%–20%), at least at the size contrasts of 8–10 that are relevant for the considered microstructure.

The underlying reason for the substantial underprediction of the effective stiffness is not fully clear at the present moment (and calls for further investigation). The following two hypotheses can be suggested: (i) Intergranular crack density  $\rho_i$  increases in the process of loading (alongside with propagation of the zigzag cracks) bringing  $\rho_i/\rho_*$  closer to its saturation value and (ii) there could be more zigzag cracks than one can identify in the photomicrograph of Figure 6, in spite of its relatively good resolution.

Yet another factor contributing to certain inherent “fuzziness” of relating the crack density to the information available in photomicrographs is that the information has the 2D character and the zigzag cracks are considered in the 2D framework, whereas the actual crack geometries are three-dimensional. High resolution computer tomography (or X-ray microscopy) may provide further insight in this matter and is a subject for future work.

## 6 | CONCLUSIONS

Experiments done on aluminum titanate specimens demonstrated that the stress–strain behavior of these ceramics exhibits nonlinearity under tension and hysteresis in loading–unloading cycles. These features are quantitatively modeled and explicitly related to microcrack density. The latter comprises two types of microcracks: cooling-induced intergranular microcracks (due to heterogeneity and anisotropy of thermal expansion) that have sizes of the order of grain diameters and much larger loading-induced microcracks of the zigzag shapes. The two produce distinctly different effects on the overall stress–strain behavior. These effects are explicitly expressed in terms of the corresponding crack densities. Our model allows monitoring the evolution of microcracking on the

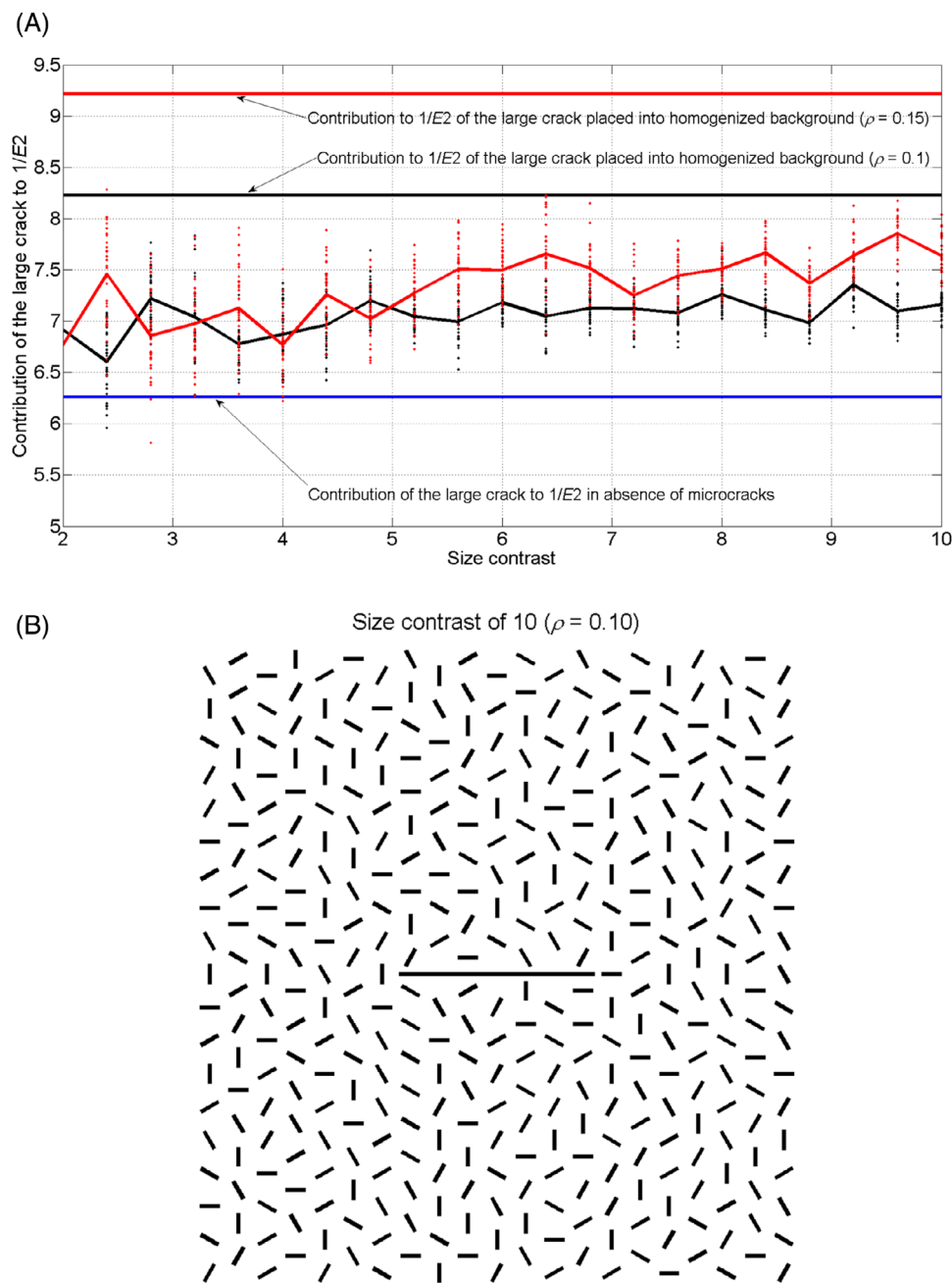


**FIGURE 12** (a) Contribution of a large crack surrounded by a cloud of smaller cracks with size ratio 1/10. (b) Sketch of the 2D crack surrounded by the array of small cracks; the 2D crack density is 0.10. Testing the hypothesis that the effect of small cracks on the compliance contribution of a large crack can be simulated by placing the latter into a homogenized environment, as a function of contrast in sizes of the large and the small cracks.

basis of stress–strain curves and explains the load–unload hysteresis of the stress–strain curves.

#### ACKNOWLEDGMENTS

This study was conducted within the framework of the HoTMiX international academic research program (Micromechanical behavior of nanostructured oxides at very high temperatures) funded by the French National Research Agency's (grant number ANR 19 CE09 0035) and

Deutsche Forschungsgemeinschaft (grant number DFG 431178689). We also thank HZB colleagues for their support as well as Ralf Britzke and Thomas Wolk (BAM) for their assistance during beam time at BAMline.

Open access funding enabled and organized by Projekt DEAL.

#### ORCID

Giovanni Bruno  <https://orcid.org/0000-0001-9632-3960>

## REFERENCES

- Bayer G. Thermal expansion characteristics and stability of pseudobrookite-type compounds,  $\text{Me}_3\text{O}_5$ . *J Less-Common Met.* 1971;24(2):129–38.
- Mouiya M, Tessier-Doyen N, Tamraoui Y, Alami J, Huger M. High temperature thermomechanical properties of a microcracked model refractory material: a silica-doped aluminium titanate. *Ceram Int.* 2023;49(14):24572–80.
- Ogunwumi SB. Strontium feldspar aluminium titanate for high temperature applications, Patent No. US6620751B1. Corning, NY: Corning Incorporated; 2003.
- Bristow JR. Microcracks, and the static and dynamic elastic constants of annealed and heavily cold-worked materials. *Br J Appl Phys.* 1960;11(2):81–5.
- Gao Z, Zimmerman JW, Kachanov M. On microstructural mechanisms causing non-linear stress-strain behavior of porous ceramics under tension. *Int J Fract.* 2013;183:283–8.
- Bruno G, Kachanov M, Sevostianov I, Shyam A. Micromechanical modeling of non-linear stress-strain behavior of polycrystalline microcracked materials under tension. *Acta Mater.* 2019;164:50–9.
- Martynyuk M, Kachanov M. Elastic compliances of the “zigzag” and intergranular cracks. *Int J Eng Sci.* 2022;171:14.
- Ohya Y, Nakagawa Z. Measurement of crack volume due to thermal expansion anisotropy in aluminium titanate ceramics. *J Mater Sci.* 1996;31(6):1555–9.
- Kakroudi MG, Yeugo-Fogaing E, Huger M, Gault C, Chotard T. Influence of the thermal history on the mechanical properties of two alumina based castables. *J Eur Ceram Soc.* 2009;29(15):3197–204.
- Hentschel MP, Hosemann R, Lange A, Uther B, Bruckner R. Small-angle X-ray refraction in metal wires, glass-fibers and hard-elastic propylenes. *Acta Crystallogr, Sect A.* 1987;43:506–13.
- Hentschel MP, Harbich K-W, Lange A. Nondestructive evaluation of single fibre debonding in composites by X-ray refraction. *NDT & E Int.* 1994;27(5):275–80.
- Müller BR, Lange A, Harwardt M, Hentschel MP. Synchrotron-based micro-CT and refraction-enhanced micro-CT for non-destructive materials characterisation. *Adv Eng Mater.* 2009;11(6):435–40.
- Görner W, Hentschel MP, Müller BR, Riesemeier H, Krumrey M, Ulm G, et al. BAMline: the first hard X-ray beamline at BESSY II. *Nucl Instrum Methods Phys Res, Sect A.* 2001;467:703–6.
- Markötter H, Müller BR, Kupsch A, Evsevlev S, Arlt T, Ulbricht A, et al. A review of the X-ray Imaging at the BAMline (BESSY II). *Adv Eng Mater.* 2023;25(11):2201034.
- Chapman D, Thomlinson W, Johnston RE, Washburn D, Pisano E, Gmur N, et al. Diffraction enhanced x-ray imaging. *Phys Med Biol.* 1997;42(11):2015–25.
- Arfelli F, Astolfo A, Rigon L, Menk RH. A Gaussian extension for diffraction enhanced imaging. *Sci Rep.* 2018;8:362.
- Kupsch A, Lange A, Hentschel MP, Onel Y, Wolk T, Staude A, et al. Evaluating porosity in cordierite diesel particulate filter materials, Part 1. X-ray refraction. *J Ceram Sci Tech.* 2013;4(4):169–75.
- Kupsch A, Müller BR, Lange A, Bruno G. Microstructure characterisation of ceramics via 2D and 3D X-ray refraction techniques. *J Eur Ceram Soc.* 2017;37(5):1879–89.
- Müller BR, Cooper RC, Lange A, Kupsch A, Wheeler M, Hentschel MP, et al. Stress-induced microcrack density evolution in beta-eucryptite ceramics: experimental observations and possible route to strain hardening. *Acta Mater.* 2018;144:627–41.
- Kupsch A, Laquai R, Müller BR, Paciornik S, Horvath J, Tushev K, et al. Evolution of damage in all-oxide ceramic matrix composite after cyclic loading. *Adv Eng Mater.* 2021;24:2100763.
- Nellesen J, Laquai R, Müller BR, Kupsch A, Hentschel MP, Anar NB, et al. In situ analysis of damage evolution in an  $\text{Al}/\text{Al}_2\text{O}_3$  MMC under tensile load by synchrotron X-ray refraction imaging. *J Mater Sci.* 2018;53(8):6021–32.
- Kupsch A, Trappe V, Müller BR, Bruno G. Evolution of CFRP stress cracks observed by in-situ X-ray refractive imaging. *IOP Conf Ser: Mater Sci Eng.* 2020;942:012035.
- Serrano-Munoz I, Roveda I, Kupsch A, Müller BR, Bruno G. Synchrotron X-ray refraction detects microstructure and porosity evolution during in-situ heat treatments. *Mater Sci Eng: A.* 2022;838:142732.
- Laquai R, Schaupt T, Griesche A, Müller BR, Kupsch A, Hannemann A, et al. Quantitative analysis of hydrogen-assisted microcracking in duplex stainless steel through X-ray refraction 3D imaging. *Adv Eng Mater.* 2022;24:2101287.
- Zocca A, Müller BR, Laquai R, Kupsch A, Wieder F, Benemann S, et al. Microstructural characterization of AP40 apatite-wollastonite glass-ceramic. *Ceram Int.* 2023;49(8):12672–9.
- Rack A, Zabler S, Müller BR, Riesemeier H, Weidemann G, Lange A, et al. High resolution synchrotron-based radiography and tomography using hard X-rays at the BAMline (BESSY II). *Nucl Instrum Methods Phys Res, Sect A.* 2008;586(2):327–44.
- Lange A, Hentschel MP, Kupsch A, Müller BR. Numerical correction of X-ray detector backlighting. *Int J Mater Res.* 2012;103(2):174–8.
- Al-Falahat AM, Kupsch A, Hentschel MP, Lange A, Kardjilov N, Markötter H, Manke I. Correction approach of detector backlighting in radiography. *Rev Sci Instrum.* 2019;90(12):125108.
- Mani D, Kupsch A, Müller BR, Bruno G. Diffraction enhanced imaging analysis with pseudo-Voigt fit function. *J Imaging.* 2022;8(8):206.
- Schneider CA, Rasband WS, Eliceiri KW. NIH image to ImageJ: 25 years of image analysis. *Nat Methods.* 2012;9(7):671–5.
- Cabeza S, Müller BR, Pereyra R, Fernandez R, Gonzalez-Doncel G, Bruno G. Evidence of damage evolution during creep of Al-Mg alloy using synchrotron X-ray refraction. *J Appl Crystallogr.* 2018;51:420–7.
- Cleveland JJ, Bradt RC. Grain size thermal expansion anisotropy effects on strength and fracture of pseudo-brookites. *Am Ceram Soc Bull.* 1976;55(4):396–6.
- Cleveland JJ, Bradt RC. Grain size/microcracking relations for pseudobrookite oxides. *J Am Ceram Soc.* 1978;61(11–12):478–81.
- Lehner F, Kachanov M. On modelling of ‘winged’ cracks forming under compression. *Int J Fract.* 1996;77(4):R69–75.
- Bruno G, Kachanov M. Microstructure-property connections for porous ceramics: the possibilities offered by micromechanics. *J Am Ceram Soc.* 2016;99(12):3829–52.
- Bruno G, Kilali Y, Efremov AM. Impact of the non-linear character of the compressive stress-strain curves on thermal and

- mechanical properties of porous microcracked ceramics. *J Eur Ceram Soc.* 2013;33(2):211–9.
37. Bruno G, Kachanov M. On modeling of microstresses and microcracking generated by cooling of polycrystalline porous ceramics. *J Eur Ceram Soc.* 2013;33(10):1995–2005.
38. Bruno G, Kachanov M. Porous microcracked ceramics under compression: micromechanical model of non-linear behavior. *J Eur Ceram Soc.* 2013;33(11):2073–85.
39. Bruno G, Garlea VO, Muth J, Efremov AM, Watkins TR, Shyam A. Microstrain temperature evolution in beta-eucryptite ceramics: measurement and model. *Acta Mater.* 2012;60(12):4982–96.
40. Buljak V, Bruno G. Numerical modeling of thermally induced microcracking in porous ceramics: an approach using cohesive elements. *J Eur Ceram Soc.* 2018;38(11):4099–108.
41. Fensch-Kleemann E, Harbich K-W, Hentschel MP. Microstructural characterisation of porous ceramics by X-ray refraction topography. *CFI Ceram Forum Int.* 2002;79(11):E35–8.
42. Grechka V, Kachanov M. Effective elasticity of rocks with closely spaced and intersecting cracks. *Geophysics.* 2006;71(3):D85–91.
43. Kachanov M, Sevostianov I. *Micromechanics of materials, with applications.* Dordrecht: Springer; 2018.
44. Mear ME, Sevostianov I, Kachanov M. Elastic compliances of non-flat cracks. *Int J Solids Struct.* 2007;44(20):6412–27.
45. Grechka V, Kachanov M. Effective elasticity of fractured rocks: a snapshot of the work in progress. *Geophysics.* 2006;71(6):W45–58.
46. Sevostianov I, Kachanov M. On the effective properties of polycrystals with intergranular cracks. *Int J Solids Struct.* 2019;156:243–50.
47. Hill R. Elastic properties of reinforced solids—some theoretical principles. *J Mech Phys Solids.* 1963;11(5):357–72.
48. Kachanov M, Tsukrov I, Shafiro B. Effective moduli of solids with cavities of various shapes. *Appl Mech Rev.* 1994;47(1):S151–74.
49. Kachanov M. Elastic solids with many cracks—a simple method of analysis. *Int J Solids Struct.* 1987;23(1):23–43.

**How to cite this article:** Mouiya M, Martynyuk M, Kupsch A, Laquai R, Müller BR, Tessier Doyen N, et al. The stress–strain behavior of refractory microcracked aluminum titanate: The effect of zigzag microcracks and its modeling. *J Am Ceram Soc.* 2023;106:6995–7008.  
<https://doi.org/10.1111/jace.19325>